Effect of post-welding sensitization on the degree of sensitization of the welding zones of AISI 304 resistance spot welding joints studied by using an electrochemical minicell

Pilar De Tiedra[a], Óscar Martín[b,*]

[a] Ciencia de los Materiales e Ingeniería Metalúrgica. Departamento CMeIM/EGI/ICGF/IM/IPF. Universidad de Valladolid. Escuela de Ingenierías Industriales. Paseo del Cauce 59, 47011, Valladolid, Spain.

[b] Ingeniería de los Procesos de Fabricación. Departamento CMeIM/EGI/ICGF/IM/IPF. Universidad de Valladolid. Escuela de Ingenierías Industriales. Paseo del Cauce 59, 47011, Valladolid, Spain.

[*] Corresponding author. Ph.: +34-983185037, E-mail: oml@uva.es (Ó. Martín)

Abstract

In resistance spot welding (RSW) joints of austenitic stainless steel (ASS), a small-scale electrochemical cell (minicell) was used for assessing individually, on each of the three welding zones, of size less than 1000 μm (fusion zone (FZ), heat affected zone (HAZ), and base metal (BM)), the combined effect of a RSW process and post-welding sensitization on the degree of sensitization (DOS). The results show that the three welding zones have different microstructures that make each of them respond differently to post-welding sensitization. The DOS varies with post-welding sensitization time in all three welding zones, but it varies at a different rate in each welding zone (the highest rate in the FZ). This variation is due to the fact that when the DOS reaches a certain level, which is observed when plotting the reactivation charge (Q_r) versus the post-welding sensitization time, a microstructural regeneration occurs. The observation that the BM of the RSW joint without post-welding sensitization has no reactivation confirms that reactivation is only possible when the DOS reaches a certain threshold.

Keywords

Resistance spot welding process; Austenitic stainless steel; Degree of sensitization; Electrochemical minicell

1. Introduction

Resistance spot welding (RSW) is widely employed for joining metal sheets in the manufacturing of automobiles, trucks trailers, buses, recreational vehicles, office furniture and appliances, railway vehicles, airplane structures and also for aeronautical and space applications [1]. In the automotive industry, RSW, because of its low cost, high speed and high degree of adaptability for automation in mass production, is the predominant process in sheet metal joining [2–9].

Austenitic stainless steels (ASSs), in view of their good combination of (i) energy-absorption ability, due to a face-centered-cubic lattice structure of austenite stabilized at room temperature by nickel alloy additions, and (ii) corrosion resistance, due to chromium alloy additions that allow the formation of a protective layer based on chromium oxide, can be considered as an interesting option for vehicle body manufacturing in the automotive industry [10,11]. Andersson et al. [12] pointed out that crash performance and energy absorbing capability of a specific component in automotive vehicles is a combination of geometry and material properties and that, since ASSs combine excellent formability with high strength, can be press-formed into components with high stiffness and high energy absorbing capability. Capelli et al. [13] and Friesen and Cunat [14] agreed that ASSs combine high strain rate sensitivity with high formability capability (that, in turn, allows straighter designs), which promotes crushing instead of buckling and, consequently, improves the energy absorption capability. The NGV (Next Generation Vehicle) Project showed that ASSs can be used to improve safety and sustainability in structural automotive systems while reducing both weight and costs [15]. In addition to the automotive industry, RSW of ASS, given its good performance, is extensively used in metro and railway car body manufacturing [16–18].

The heat associated with welding processes may cause, in ASSs, a phenomenon known as sensitization which leads to precipitation, along critical zones, of chromium-rich phases whose adjacent zones are then chromium depleted zones and therefore more susceptible to corrosion attack [19,20]. RSW has the advantage over other welding processes of having rapid heating/cooling cycles [3,21,22], which limits the thermal exposure time and, therefore, can reduce the formation of the aforementioned chromium-rich phases [23,24].

Even though the degree of sensitization (DOS) associated with RSW process is low [25], the RSW joint may be subjected to high temperature service conditions [15,26] where the temperature range in which sensitization occurs is reached and, hence, it is necessary to assess the combined effect of RSW process and post-welding sensitization, induced by subsequent service conditions, on the DOS [25]. In addition, the effect of corrosion can be critical in an already small-sized welded joint such as a RSW joint [27].

Electrochemical potentiokinetic reactivation (EPR) is a quasi non-destructive test that is used mainly to assess the DOS, and which is more sensitive, faster, and more precise than the conventional corrosion tests [28,29].

RSW is a fusion welding process, in which a weld nugget is formed from the solidification of the molten metal after a heating by Joule effect [30]. Thus, as a result of the process, three weld zones can be distinguished in the RSW joint [31]: (i) fusion zone (FZ), also called weld nugget; (ii) heat affected zone (HAZ); and (iii) base metal (BM). Since the maximum dimensions of the FZ are limited by the face diameter of the contact electrodes (i.e., by the electrode-sheet contact area) and by the thickness of the overlapped sheets, and since the HAZ is narrow due to the fact that RSW is a low heat input process compared to other welding processes [32,33] such as gas metal arc welding (GMAW) process [34], and that ASSs have low thermal conductivity [35] compared to carbon steel [36,37], a conventional large-scale EPR test may not be able to isolate specific results from each of the three small-sized individual zones of the RSW joint.

The majority of microelectrochemical methods employed to study localized corrosion on small areas [38–42] use microcapillary-based droplet cells that have the advantage of the small size (in the micrometer range) of the exposed working area [43–45]. These capillary microcells have some drawbacks [46] and in some cases it is not required to use areas as small as those provided by microcapillaries [47]. Thus, ad hoc small-scale electrochemical cell known as “minicell”, different to the capillary-based microcell and which has been successfully utilized in the study of welded joints of ASSs [47–50], can be applied to RSW joints given that it has study sizes in the range of 200–1000 μm [49].

In this work, a small-scale electrochemical cell (minicell) was used for assessing individually, on each of the three small-sized zones of the welded joint, the combined effect of RSW process and post-welding sensitization, induced by subsequent service conditions, on the DOS, with the aim of overcoming the limitations of employing large-scale EPR tests for assessing the DOS in small-sized welding zones.

2. Experimental Procedure

2.1. Materials

Table 1 shows the chemical composition of the AISI 304 ASS sheets (with 0.8 mm thickness) welded by RSW process and Table 2 summarizes their mechanical properties.

Table 1. Chemical composition of the AISI 304 ASS sheets (wt. %).

C	S	P	Al	Co	W	Si	Mn
0.08	0.002	0.019	0.003	0.17	0.03	0.426	1.153
Ti	V	Cu	Nb	Mo	Cr	Ni	Fe
0.004	0.05	0.39	0.02	0.36	18.03	8.74	Bal.

Table 2. Mechanical properties of the AISI 304 ASS sheets.

Tensile strength (MPa)	Yield strength (MPa)	Microhardness (HV, 100g)	Total elongation (%)
675	290	162	70

2.2. RSW procedure

The AISI 304 ASS sheets were welded with a single-phase alternating current (AC) 50 Hz equipment by using water-cooled truncated cone Resistance Welding Manufacturing Alliance (RWMA) Group A Class 2 electrodes with 4.5 mm face diameter [51]. The controlled parameters in RSW process were welding current (fixed at 5 kA), welding time (fixed at 0.20 s), and electrode force (fixed at 1500 N).

As a result of the fusion welding process, the RSW joint has three small-sized welding zones with different microstructures that can respond in different ways to post-welding sensitization: (i) FZ (weld nugget), which is a cast dendritic microstructure of austenite with delta-ferrite in interdendritic regions (Fig. 1); (ii) HAZ, whose microstructure depends on the heat generated in the RSW process which may remove signs of prior cold work (Fig. 2); and (iii) BM, which is not affected by the welding heat input, and shows an austenitic structure with signs of prior cold work such as delta-ferrite bands oriented in the rolling direction (Fig. 3) [19,25].

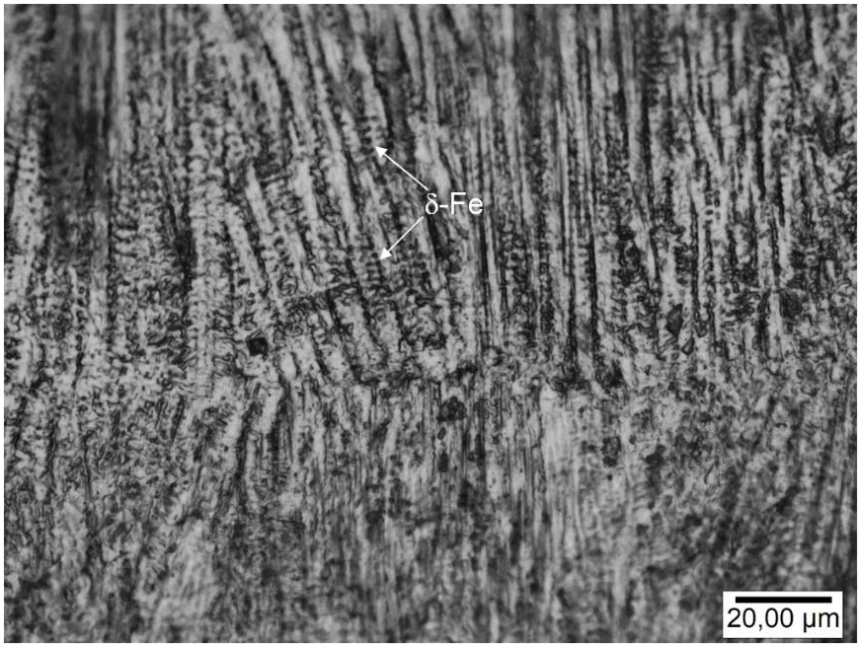

Fig. 1. Optical micrograph of the FZ of a RSW joint (without post-welding sensitization), which has a cast dendritic microstructure of austenite with delta-ferrite (δ-Fe) in interdendritic regions (electrolytic etching with oxalic acid according to ASTM A262-15(2021) Practice A) [52].

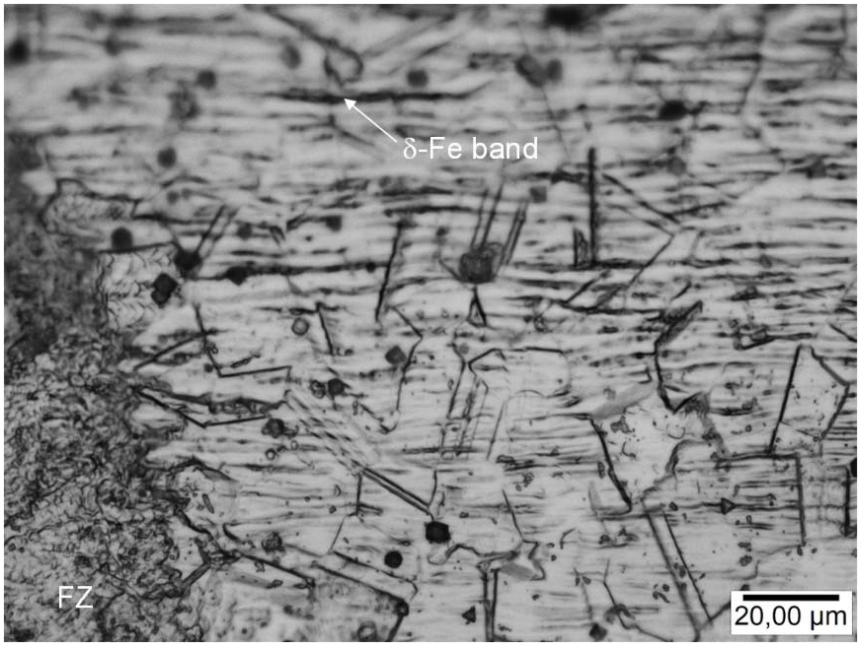

Fig. 2. Optical micrograph of the HAZ of a RSW joint (without post-welding sensitization), in which signs of prior cold work (delta-ferrite (δ-Fe) bands oriented in the rolling direction) are partially removed by the effect of the welding heat input (electrolytic etching with oxalic acid according to ASTM A262-15(2021) Practice A) [52].

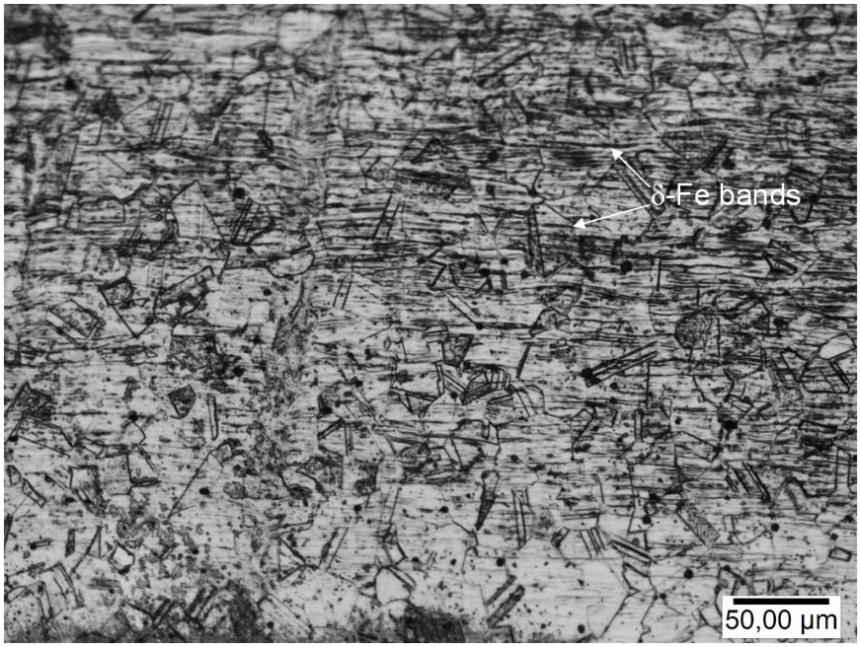

Fig. 3. Optical micrograph of the BM of a RSW joint (without post-welding sensitization), which shows an austenitic structure with signs of prior cold work such as delta-ferrite (δ-Fe) bands oriented in the rolling direction (electrolytic etching with oxalic acid according to ASTM A262-15(2021) Practice A) [52].

2.3. Post-welding sensitization procedure

Each of the twelve post-welding sensitization conditions [25] were applied on a different RSW joint, considering the RSW joint without post-weld sensitization as the reference state. Thus, a sample was obtained for each state: sample No. 0 corresponds to the RSW joint without post-weld sensitization and samples Nos. 1 to 12 correspond to RSW joints subjected to different post-weld sensitization conditions (Table 3).

Table 3. The twelve different states of RSW + post-welding sensitization compared to reference state. A sample was obtained for each state and three small-scale EPR tests were performed, by using a minicell, on each of the samples (one small-scale EPR test on each of the welding zones, i.e., FZ, HAZ and BM).

RSW condition	Post-welding sensitization conditions		Sample No.
	Temperature (ºC)	Time (min)	
Welding current = 5 kA Welding time = 0.20 s Electrode force = 1500 N	--	--	0 [a]
	675	15	1
		30	2
		45	3
		60	4
		120	5
		240	6
	750	15	7
		30	8
		45	9
		60	10
		120	11
		240	12

[a] Sample No. 0 corresponds to the reference state and has no post-welding sensitization. FZ, HAZ and BM shown respectively in Fig.1, Fig. 2, and Fig. 3, were obtained from sample No. 0.

2.4. Small-scale EPR test

2.4.1. Minicell set-up

The sample to be studied was clamped on a micrometer table. Thus, it was possible to move the sample to the desired position with respect to the tip of the minicell, so that the tip was located exactly on top of the weld zone to be studied in each case (Fig. 4A).

The minicell used (Fig. 4B) was made in polymethyl methacrylate (PMMA). It consisted of two parts: the lid and the body. The electrolyte flowed in the minicell through the upper inlet (5 mm in diameter) and left through the lower outlet (1 mm in diameter). Thus, the reduction in section led to a suction effect that continuously renovated the chemical species of the working area and allowed a continuous flow of fresh electrolyte over the working electrode area, and the disturbing phenomenon of possible

bubbling was then lessened. The platinum counter electrode (0.2 mm wire) was positioned between the working and the reference electrode. The same reference electrode as for large-scale experiments was used (Saturated Calomel Electrode (SCE)), and was located at a distance (ca. 9 mm) from the working electrode (this positioning is aimed at obtaining the best possible electrical signals) [47,49,50].

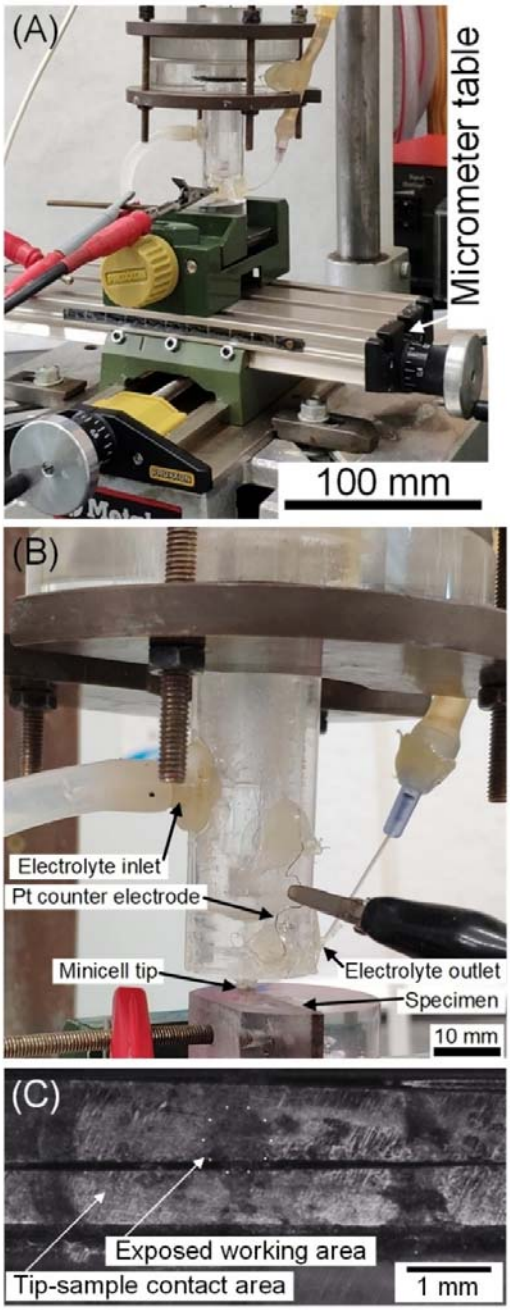

Fig. 4. (A) Micrometer table on which the sample was clamped. (B) Minicell used in the small-scale EPR tests. (C) Optical macrograph taken in the BM of a RSW joint after a small-scale EPR test to show the size of the exposed working area.

2.4.2. Small-scale EPR test procedure

EPR test was performed following ASTM Standard G-108 [53] but, given that the results were found to be dependent on the degree of surface preparation, an electrochemical conditioning, which allows a degree of surface preparation (No. 600 emery paper) less severe than the established by the aforementioned standard, was conducted [47]. The electrolyte was 0.5 M H_2SO4 + 0.01 M KSCN and the test temperature is 30 °C ± 1. The experimental procedure of the test was the following: a holding time of 5 min at open circuit (OC) potential, deaerated, an anodic attack at −220 mV(SCE) for 2 min, a holding time of 2 min at VOC, a cathodic cleaning at −600 mV(SCE) for 1 min and a holding time of 5 min at VOC. Passivation was carried out by applying 200 mV(SCE) for 2 min (a longer time would give rise to a more stable passive layer, which would prevent certain EPR curves from having a passive zone where the current density is not exactly constant, but it would also lead to a lack of reactivation in other EPR curves). The reactivation scan starts at 200 mV until 100 mV below the VOC at a rate of 100 mV/min.

As shown above (Fig 4C), the exposed working area studied in each of the small-scale EPR tests has a value of approximately 0.005 cm^2 (ca. 0.8 mm in diameter).

Three small-scale EPR tests were conducted, by using the minicell, on each of the thirteen samples Nos. 0 to 12 (one small-scale EPR test on each of the welding zones, i.e., FZ, HAZ and BM) (Fig. 5A). The repeatability of the tests was assessed by repeating the small-scale EPR test several times in the same welding zone and verifying that the differences between the EPR curves obtained were not significant (Fig. 5B).

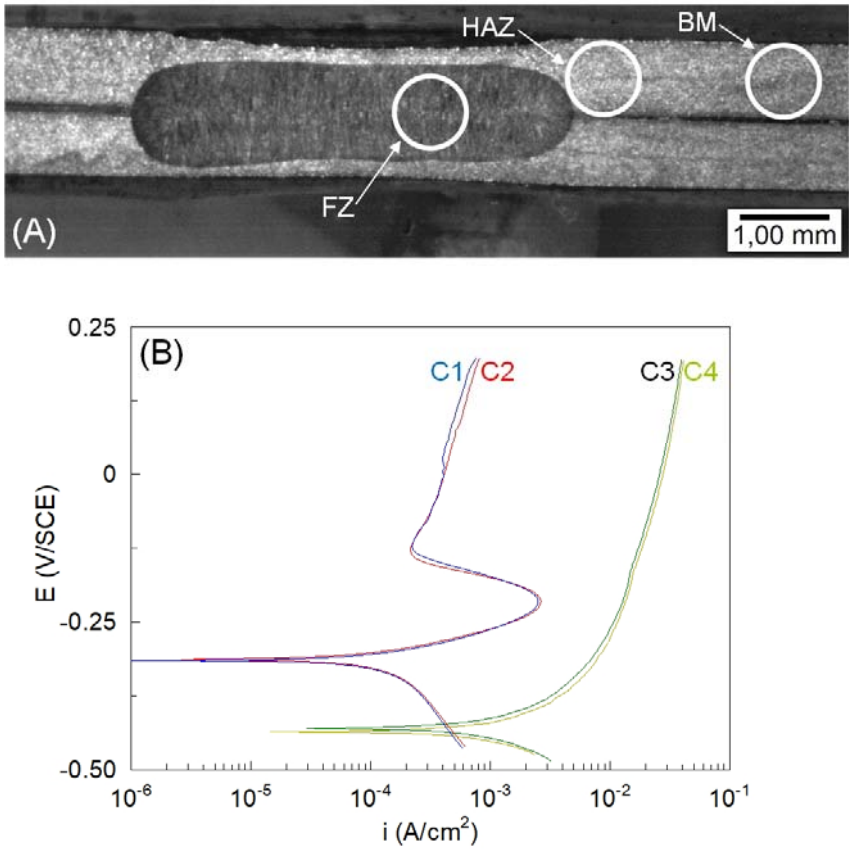

Fig. 5. (A) Location of the small-scale EPR tests in each of the welding zones. The exposed working area is indicated by a circle 0.005 cm^2 in area and 0.8 mm in diameter. in the small-scale EPR tests. The RSW joint shown corresponds to sample No. 10 (electrolytic etching with oxalic acid according to ASTM A262-15(2021) Practice A) [52]. (B) Assessment of repeatability of the small-scale EPR tests: curves obtained from the BM in samples No. 1 (C1 and C2) and No. 0 (C3 and C4).

The EPR test parameter Q_r (reactivation charge) (Fig. 6), given its correspondence with the DOS [54], is used to assess such a DOS [55].

Certain EPR small-scale EPR curves show local increases of current density that may be due to the formation of crevice corrosion at the interface between the minicell tip and the sample, but this phenomenon occurs mainly in the passive zone of the EPR curve, outside the reactivation hump (Figs. 9C, 10D and 12B) and also, as pointed out by De Tiedra [56], does not affect significantly the reactivation charge Q_r (Fig. 6).

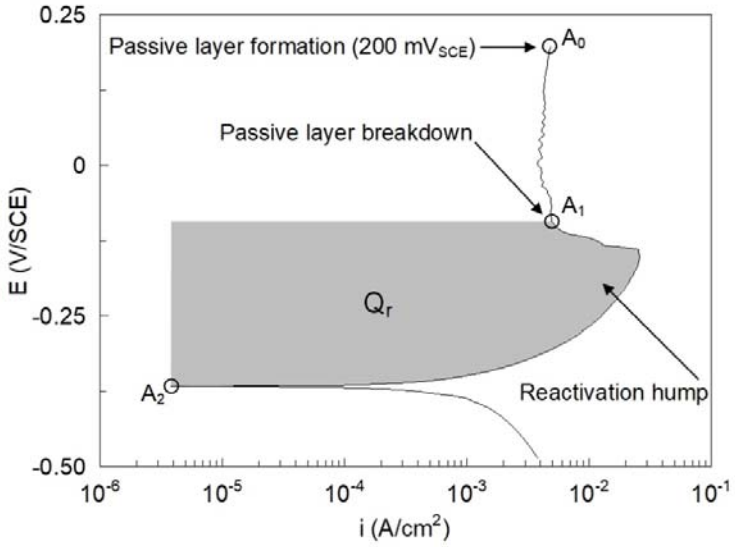

Fig. 6. In each EPR curve, the reactivation charge Q_r is determined between point A_1 and point A_2 (reactivation hump). Passive layer formation occurs at 200 mV_{sce} (A_0) and the passive layer (passive zone between A_0 and A_1) limits the flow of current until its localized breakdown (A_1) causes the current density to increase significantly. The small-scale EPR curve shown is obtained from the FZ of sample No. 11.

3. Results and Discussion

The results obtained from the small-scale EPR curves (Figs. 7-12) are analyzed in terms of the Q_r parameter (Figs. 13 and 14) [55]. As shown in Fig. 6, the Q_r parameter increases as the current density through the passive layer increases, which occurs when the passive layer is broken or weakened at the zones where chromium-rich phases precipitate.

The DOS values are, in general, higher in the post-welding sensitization at higher temperature (750 ºC) [57] (Figs. 13 and 14), which is consistent with the results of Yu et al. [58]. According to these authors, DOS increases as sensitization temperature increases, due to the fact that the rate of chromium diffusion increases when the temperature increases.

As it can be seen in Figs. 7-14, the DOS experiences a variation with post-welding sensitization time which is due to the fact that when the DOS reaches a certain level, a microstructural regeneration, during which the DOS decreases with sensitization time, takes place [49,50]. After this microstructural regeneration, the microstructure undergoes a further increase in DOS with sensitization time until the level at which microstructural regeneration occurs is reached again. These results are consistent with those of Matula et al. [55], according to which the EPR test is capable of detecting modifications in the chromium distribution, not only the depletion but also the rehomogenization [55].

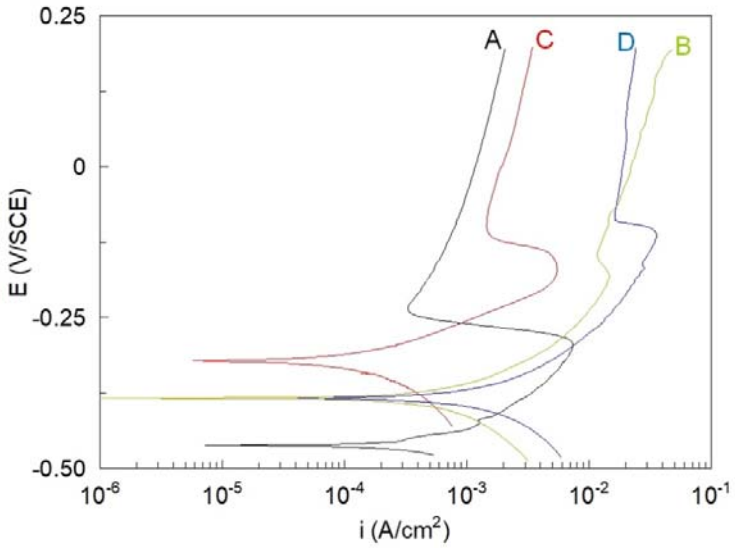

Fig. 7. Small-scale EPR curves obtained from the FZ of: (A) sample No. 0 (Q_r = 0.52144 C/cm^2); (B) sample No. 1 (Q_r = 1.2165 C/cm^2); (C) sample No. 4 (Q_r = 0.37101 C/cm^2); and (D) sample No. 6 (Q_r = 3.4622 C/cm^2).

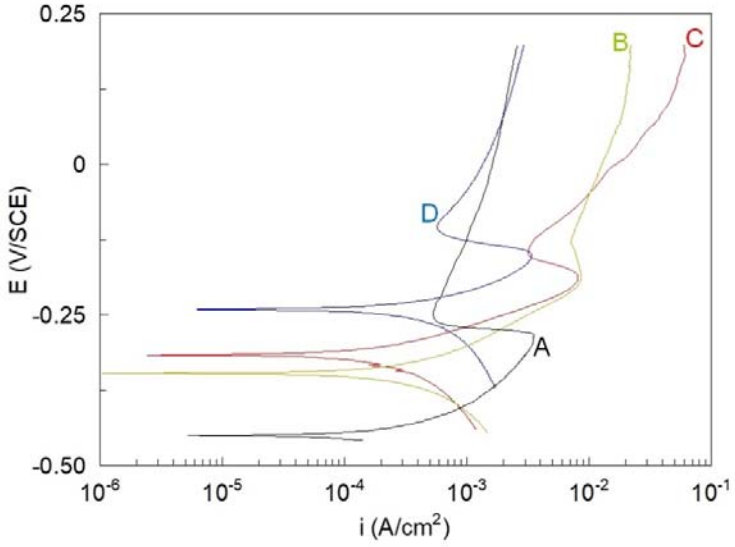

Fig. 8. Small-scale EPR curves obtained from the HAZ of: (A) sample No. 0 (Q_r = 0.23861 C/cm^2); (B) sample No. 1 (Q_r = 0.69272 C/cm^2); (C) sample No. 4 (Q_r = 0.41732 C/cm^2); and (D) sample No. 6 (Q_r = 0.1602 C/cm^2).

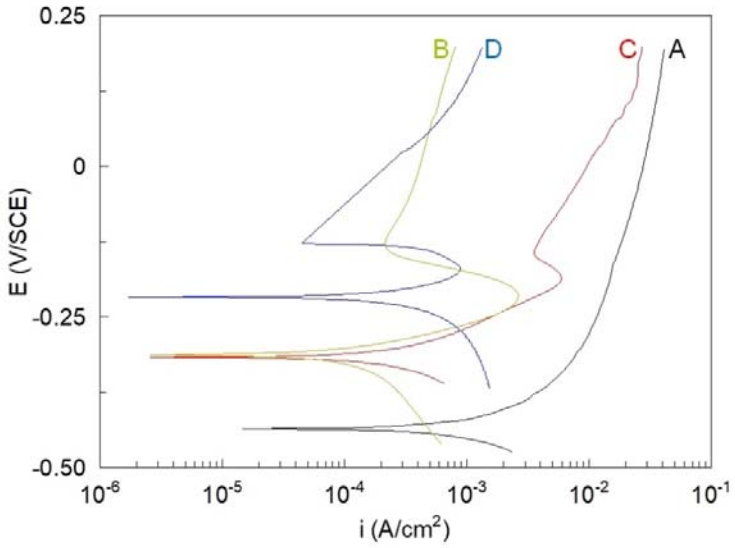

Fig. 9. Small-scale EPR curves obtained from the BM of: (A) sample No. 0 (Q_r = 0 C/cm^2, i.e., there is no reactivation); (B) sample No. 1 (Q_r = 0.14747 C/cm^2); (C) sample No. 4 (Q_r = 0.32757 C/cm^2); and (D) sample No. 6 (Q_r = 0.03397 C/cm^2).

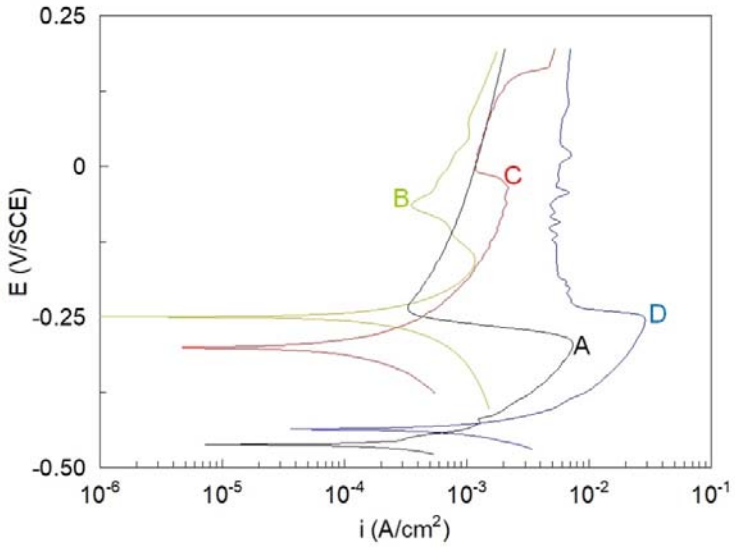

Fig. 10. Small-scale EPR curves obtained from the FZ of: (A) sample No. 0 (Q_r = 0.52144 C/cm^2); (B) sample No. 7 (Q_r = 0.094963 C/cm^2); (C) sample No. 10 (Q_r = 0.25427 C/cm^2); and (D) sample No. 12 (Q_r = 2.1729 C/cm^2).

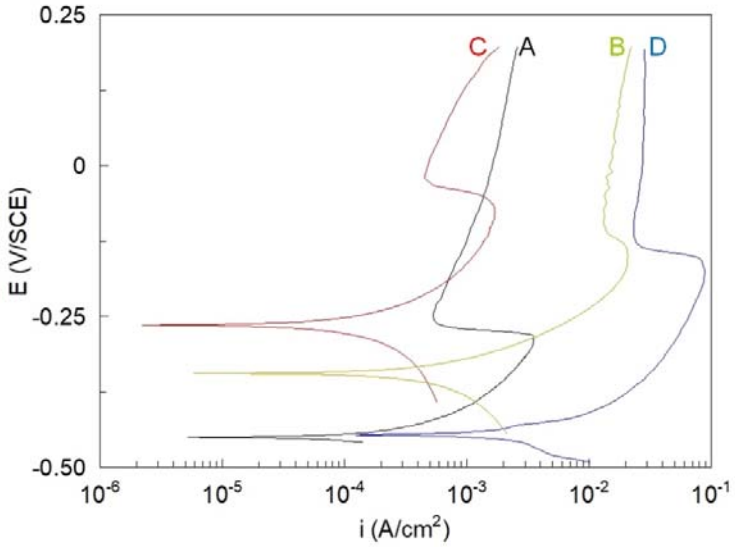

Fig. 11. Small-scale EPR curves obtained from the HAZ of: (A) sample No. 0 (Q_r = 0.23861 C/cm^2); (B) sample No. 7 (Q_r = 1.9035 C/cm^2); (C) sample No. 10 (Q_r = 0.16359 C/cm^2); and (D) sample No. 12 (Q_r = 10.345 C/cm^2).

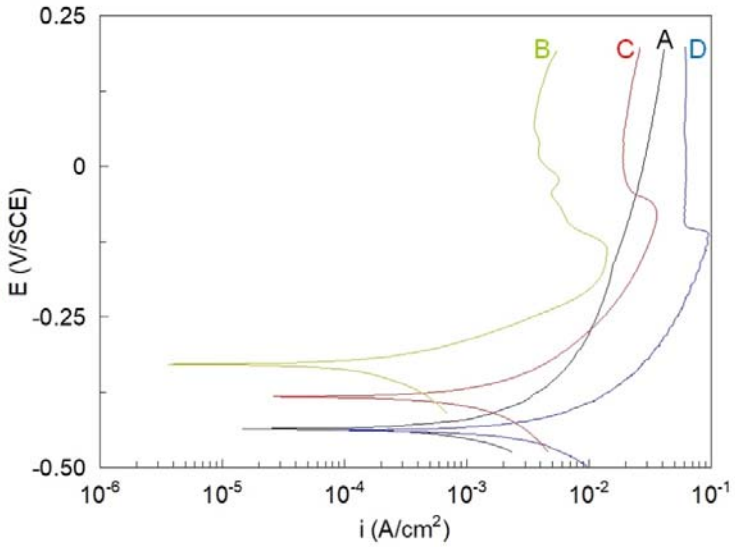

Fig. 12. Small-scale EPR curves obtained from the BM of: (A) sample No. 0 (Q_r = 0 C/cm^2, i.e., there is no reactivation); (B) sample No. 7 (Q_r = 1.1744 C/cm^2); (C) sample No. 10 (Q_r = 4.2562 C/cm^2); and (D) sample No. 12 (Q_r = 11.143 C/cm^2).

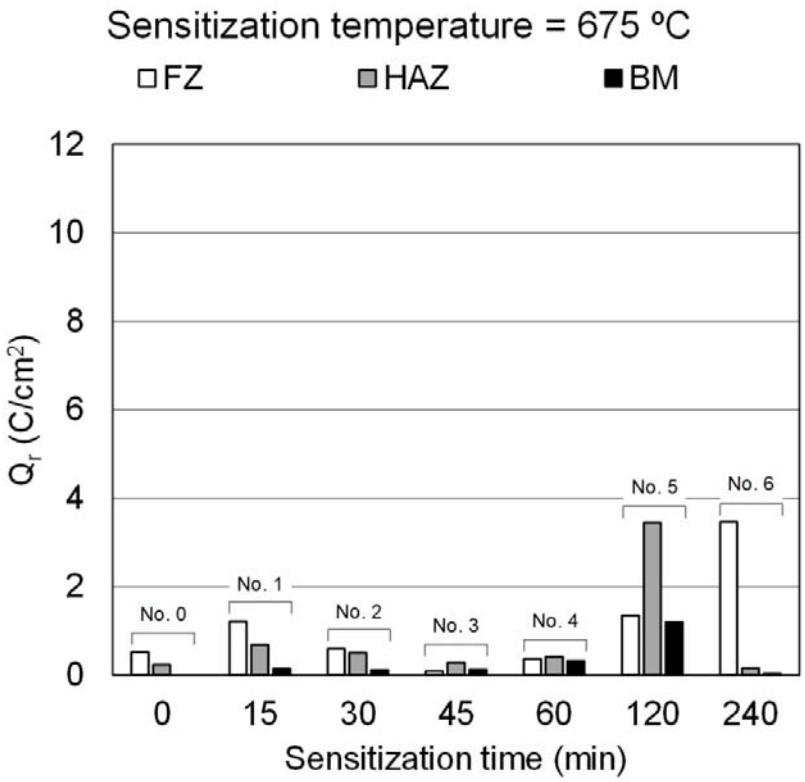

Fig. 13. Reactivation charge, Q_r (C/cm^2), obtained from each of the welding zones (FZ, HAZ and BM) of the RSW joint without post-weld sensitization (sample No. 0, which has no reactivation in the BM, i.e., with Q_r = 0 C/cm^2) and of the six RSW joints subjected to post-weld sensitization at 675 ºC (samples Nos. 1 to 6).

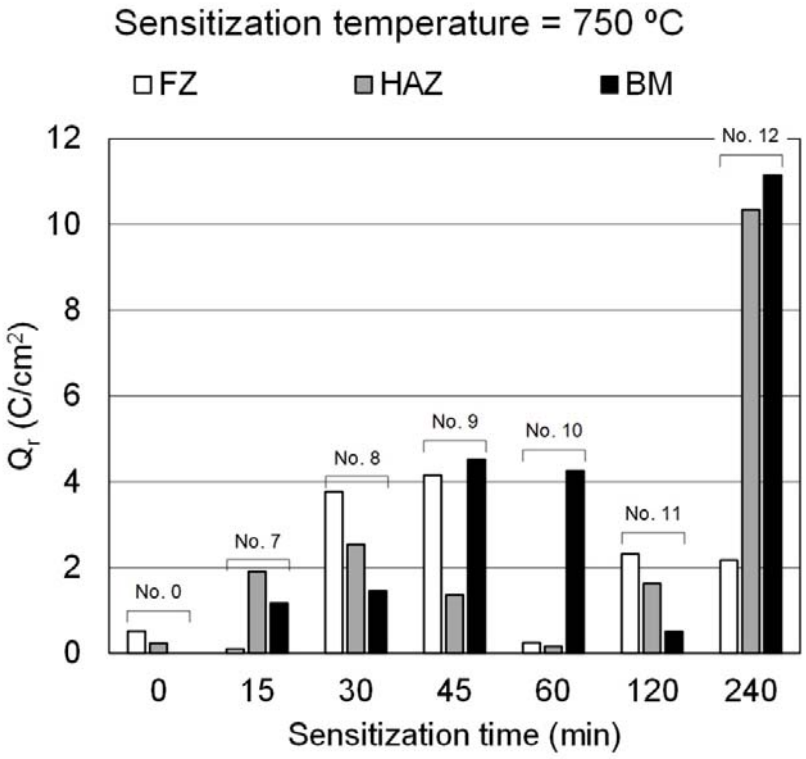

Fig. 14. Reactivation charge, Q_r (C/cm^2), obtained from each of the welding zones (FZ, HAZ and BM) of the RSW joint without post-weld sensitization (sample No. 0, which has no reactivation in the BM, i.e., with Q_r = 0 C/cm^2) and of the six RSW joints subjected to post-weld sensitization at 750 ºC (samples Nos. 7 to 12).

In FZ, the post-welding sensitization causes the precipitation of chromium (ferrite-stabilizing element) rich phases along dendritic boundaries [19] (Fig. 17), which have a high content of delta-ferrite due to the rapid cooling [59,60] associated with the RSW process [61,62]. This type of sensitization is associated with interdendritic corrosion (IDC). The variation, of the DOS in FZ, with post-weld sensitization time, shown in Figs. 13 and 14, is in accordance with that of the IDC, shown in the Figs. 1, 15 (A) to (C) and 16 (A) to (C).

In both HAZ and BM, the post-welding sensitization causes the precipitation of chromium-rich phases [19,20,35,63–65], which takes place along: (i) austenite/delta-ferrite interfaces, twins and slip bands inside austenitic grains (this type of sensitization is associated with transgranular corrosion (TGC)); and (ii) and grain boundaries (this type of sensitization is associated with intergranular corrosion (IGC)). The variation, of the DOS in HAZ and BM, with post-weld sensitization time, shown in Figs. 13 and 14, is in accordance with that of the TGC and IGC, shown in Figs. 2, 15 (D) to (F) and 16 (D) to (F) for HAZ and in Figs. 3, 15 (G) to (I) and 16 (G) to (I) for BM. It is also observed that, in both HAZ and BM, the variation over sensitization time is more significant for TGC than for IGC [25].

As it can be seen in Figs. 13 to 16, the fact that the three welding zones (FZ, HAZ and BM) have different microstructures makes each of them respond differently to post-welding sensitization:

although the DOS varies with sensitization time in all three welding zones, it varies at a different rate in each welding zone.

As it can be observed in Figs. 13 and 14, the variation rate of the DOS with post-welding sensitization time is higher in the FZ than in HAZ and BM. This phenomenon is caused by the fact that the kinetics of microstructural regeneration is faster in FZ than in HAZ and BM [25,66], which may be due to two causes. Firstly, the chemical segregation associated with the solidification processes [67,68], where the last fraction of liquid that solidifies enriches in ferrite-stabilizing elements such as chromium, and thus, the interdendritic regions can be expected to be zones for preferential delta-ferrite formation [69,70] (this chemical segregation makes the rate of diffusion higher since concentration gradient is, according to Fick's law, the driving force of diffusion [71]). Secondly, diffusion takes place faster along grain boundaries than into the grain [72,73] and, as it can be seen in Figs. 1, 2, 3, 15 and 16, grain boundary area is larger in the dendritic-grain microstructure of FZ than in the equiaxed-grain microstructure of HAZ and BM.

Finally, the fact that BM (without thermal effects due to welding process) of sample No. 0 (without post-welding sensitization) has no reactivation (EPR curve A in Fig. 9 and Fig. 12) confirms that the lack of reactivation occurs when the DOS does not reach a certain reactivation threshold [19].

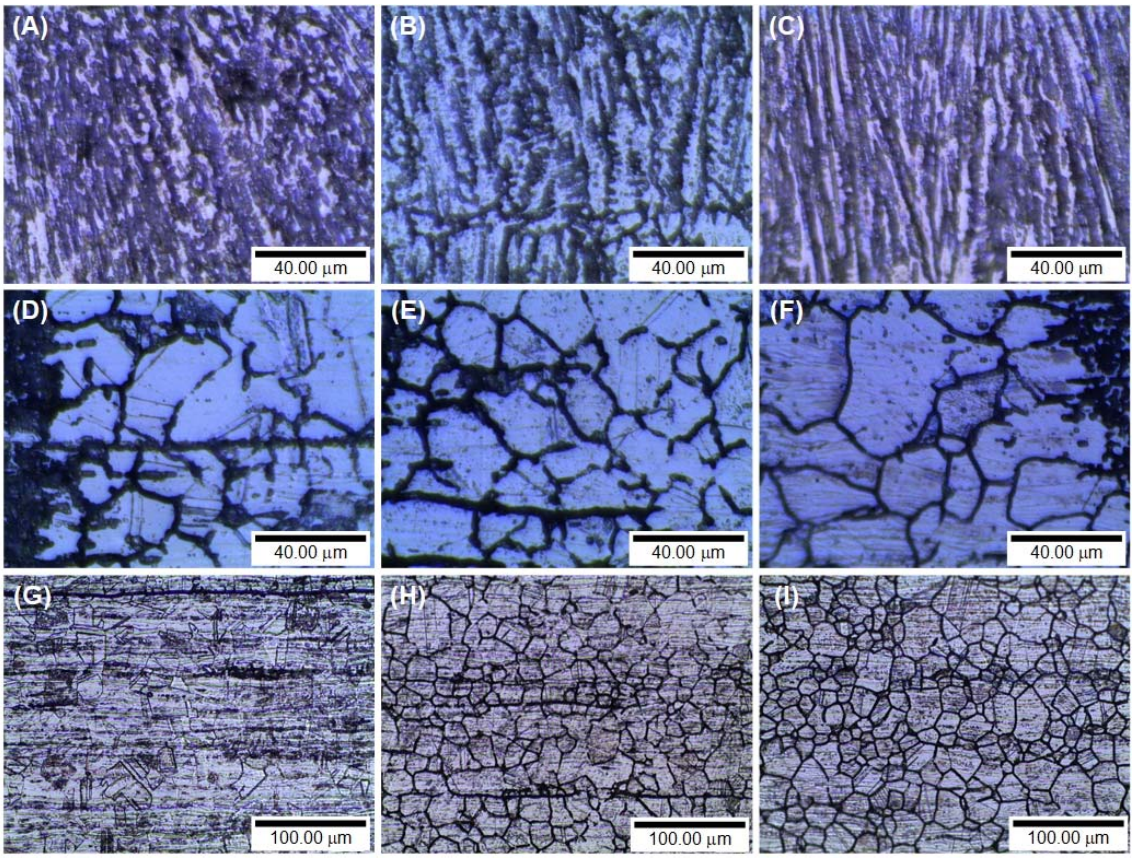

Fig. 15. Optical micrographs (electrolytic etching with oxalic acid according to ASTM A262-15(2021) Practice A [52]) of: (A) FZ of sample No. 1; (B) FZ of sample No. 4; (C) FZ of sample No. 6; (D) HAZ of sample No. 1. (E) HAZ of sample No. 4; (F) HAZ of sample No. 6; (G) BM of sample No. 1; (H) BM of sample No. 4; (C) BM of sample No. 6.

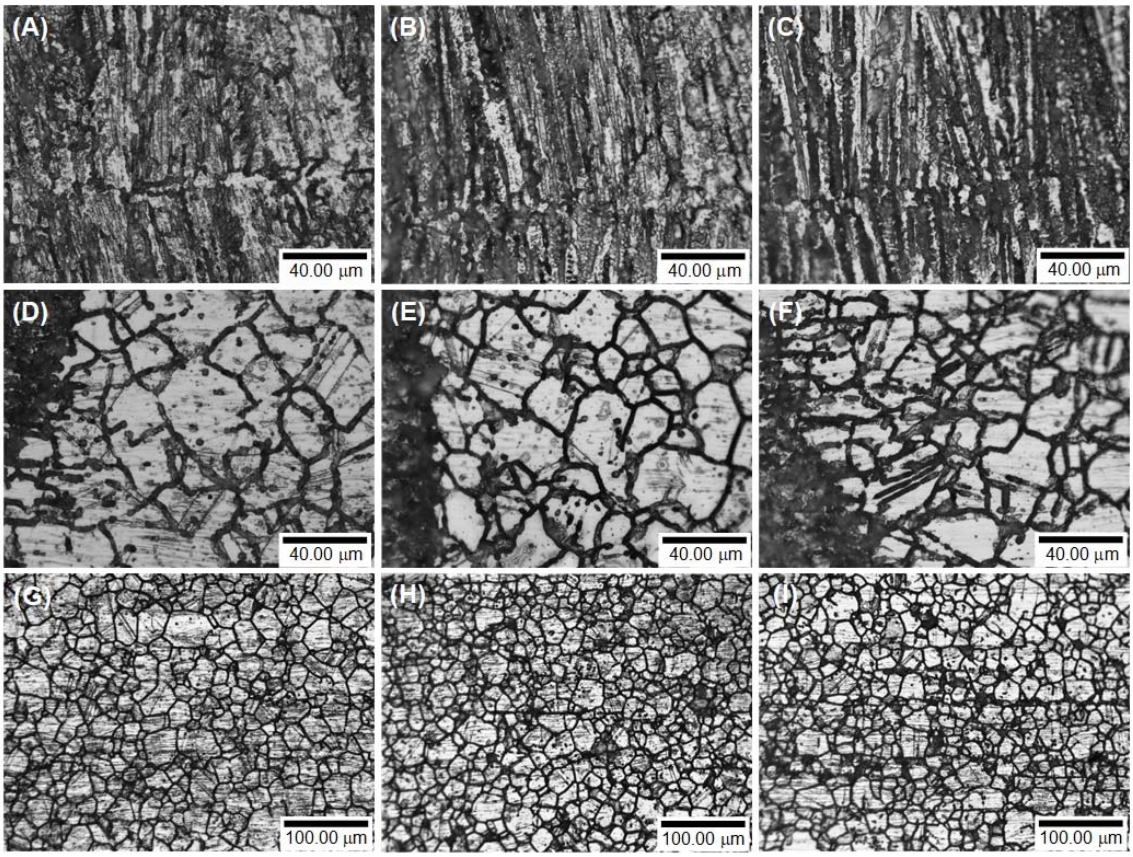

Fig. 16. Optical micrographs (electrolytic etching with oxalic acid according to ASTM A262-15(2021) Practice A [52]) of: (A) FZ of sample No. 7; (B) FZ of sample No. 10; (C) FZ of sample No. 12; (D) HAZ of sample No. 7. (E) HAZ of sample No. 10; (F) HAZ of sample No. 12; (G) BM of sample No. 7; (H) BM of sample No. 10; (C) BM of sample No. 12.

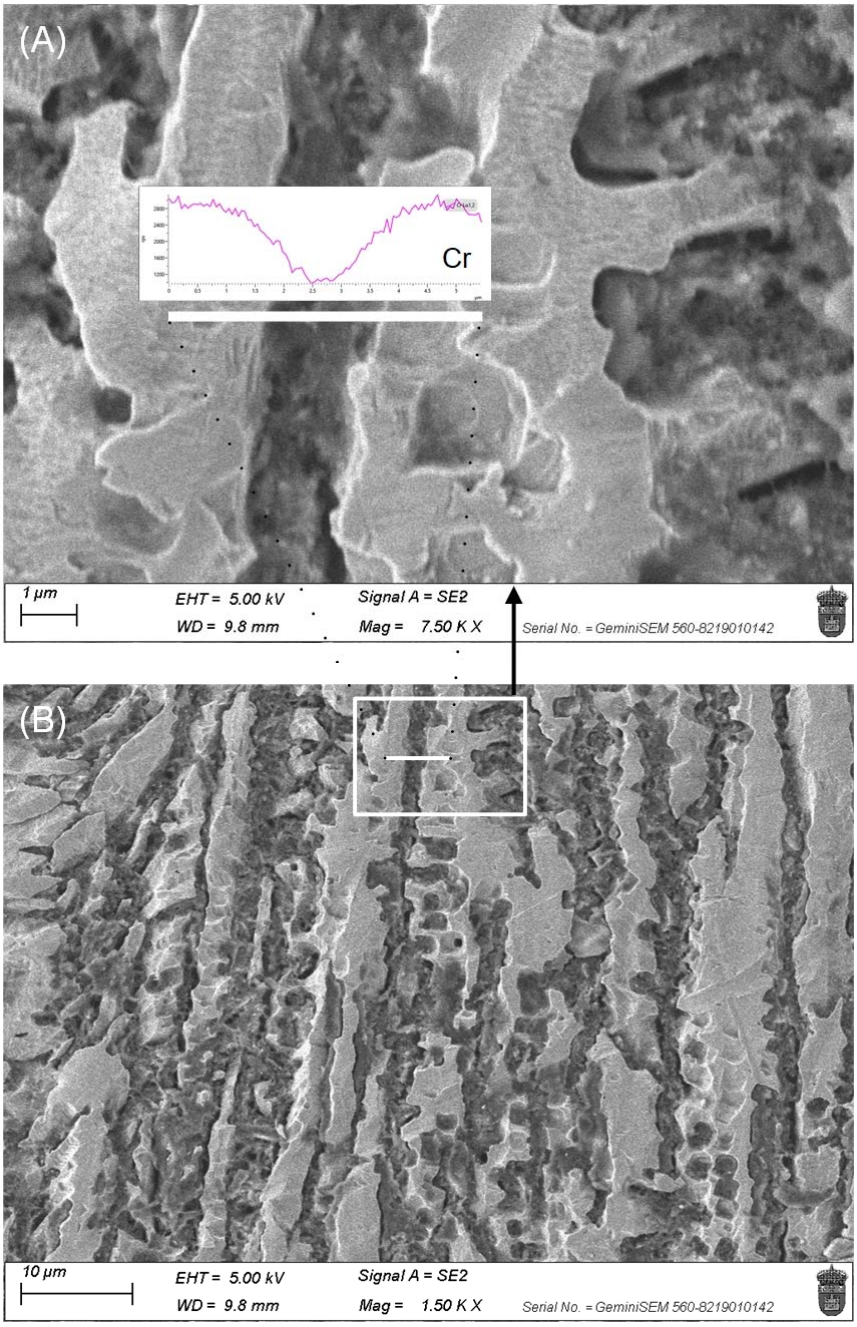

Fig. 17. (A) EDX line scan between two dendrites for Cr content in the FZ of sample No. 12; although the electrolytic etching with oxalic acid, according to ASTM A262-15(2021), dissolves the chromium-rich phases that had precipitated along interdendritic regions, the chromium depleted zones, adjacent to the chromium-rich phases, are shown. (B) SEM micrograph of the line scan location.

Conclusions

In this work, a small-scale electrochemical cell (minicell) is used for assessing individually, on each of the three small-sized zones (of size less than 1000 µm) of the welded joint, the combined effect of RSW process and post-welding sensitization, induced by subsequent service conditions, on the DOS. The main conclusions are:

- The three weld zones (FZ, HAZ and BM) in the RSW joint have different microstructures that makes each of them respond differently to post-welding sensitization: although the DOS varies with post-welding sensitization time in all three weld zones, it varies at a different rate in each weld zone.
- The variation of the DOS with post-welding sensitization time observed is due to the change when the DOS reaches a certain level (which can be observed when plotting the reactivation charge (Q_r) versus the post-welding sensitization time) and a microstructural regeneration occurs.
- The variation rate of the DOS with post-welding sensitization time is higher in the FZ than in HAZ and BM. This phenomenon may be due to kinetics of microstructural regeneration are faster in FZ than in HAZ and BM.
- The base metal (without thermal effects due to welding process or post-welding sensitization) has no reactivation appears to confirm that reactivation of the RSW weld microstructures only occurs when the DOS reaches a certain reactivation threshold.

Disclosure statement

No potential conflict of interest was reported by the author(s).

ORCID

Pilar De Tiedra: https://orcid.org/0000-0003-2026-3476

Óscar Martín: https://orcid.org/0000-0001-9200-5797

References

[1] Zhou K, Yao P. Overview of recent advances of process analysis and quality control in resistance spot welding. Mech Syst Signal Process 2019;124:170–98. https://doi.org/10.1016/j.ymssp.2019.01.041.

[2] Zhang Y, Xu W, Zhang G, Tao W, Yang S. Mechanical Behavior and Failure Mechanism of Q&P980 Steel During In Situ Post-Weld Heat Treatment (PWHT) Resistance Spot Welding. Metall Mater Trans A Phys Metall Mater Sci 2022;53:794–809. https://doi.org/10.1007/s11661-021-06546-5.

[3] Tamizi M, Pouranvari M, Movahedi M. The Role of HAZ Softening on Cross-Tension Mechanical Performance of Martensitic Advanced High Strength Steel Resistance Spot Welds. Metall Mater Trans A 2021;52:655–67. https://doi.org/10.1007/s11661-020-06104-5.

[4] Soomro IA, Pedapati SR, Awang M. A review of advances in resistance spot welding of automotive sheet steels: emerging methods to improve joint mechanical performance. Int J Adv Manuf Technol 2022;118:1335–66. https://doi.org/10.1007/s00170-021-08002-5.

[5] Nadimi N, Yadegari R, Pouranvari M. Resistance Spot Welding of Quenching and Partitioning (Q&P) Third-Generation Advanced High-Strength Steel: Process–Microstructure–Performance. Metall Mater Trans A Phys Metall Mater Sci 2023;54:577–89. https://doi.org/10.1007/s11661-022-06903-y.

[6] Martin O, Ahedo V, Santos JI, Galan JM. Comparative Study of Classification Algorithms for Quality Assessment of Resistance Spot Welding Joints From Pre- and Post-Welding Inputs. IEEE Access 2022;10:6518–27. https://doi.org/10.1109/ACCESS.2022.3142515.

[7] Becker N, Gilgert J, Petit EJ, Azari Z. The effect of galvanizing on the mechanical resistance and fatigue toughness of a spot welded assembly made of AISI410 martensite. Mater Sci Eng A 2014;596:145–56. https://doi.org/10.1016/j.msea.2013.12.008.

[8] Aghajani H, Pouranvari M. Influence of In Situ Thermal Processing Strategies on the Weldability of Martensitic Stainless Steel Resistance Spot Welds: Effect of Second Pulse Current on the Weld Microstructure and Mechanical Properties. Metall Mater Trans A 2019;50:5191–209. https://doi.org/10.1007/s11661-019-05443-2.

[9] Ahedo V, Martín Ó, Santos JI, De Tiedra P, Galán JM. Independence of EPR and PAP tests performed on resistance spot welding joints. Corros Eng Sci Technol 2017:1–7. https://doi.org/10.1080/1478422X.2017.1319148.

[10] Zhang Y, Guo J, Li Y, Luo Z, Zhang X. A comparative study between the mechanical and microstructural properties of resistance spot welding joints among ferritic AISI 430 and austenitic AISI 304 stainless steel. J Mater Res Technol 2020;9:574–83. https://doi.org/10.1016/j.jmrt.2019.10.086.

[11] Feng QB, Li YB, Carlson BE, Lai XM. Study of resistance spot weldability of a new stainless steel. Sci Technol Weld Join 2019;24:101–11. https://doi.org/10.1080/13621718.2018.1491378.

[12] Andersson R, Schedin E, Magnusson C, Ocklund J, Persson A. The Applicability of Stainless Steel for Crash Absorbing Components. SAE Trans. Sect. 6 J. Passeng. CAR Mech. Syst. J., vol. 111, 2002, p. 1918–22. https://doi.org/10.4271/2002-01-2020.

[13] Capelli F, Boneschi V, Viganò P. Stainless Steel: a new structural automotive material. 9th Int. Conf. Exhib. FLORENCE ATA, 2005.

[14] Friesen F, Cunat P-J. Application of Stainless Steel in Crash Structures of Vehicles. SAE Trans. Sect. 5 J. Mater. Manuf., vol. 113, 2004, p. 428–32. https://doi.org/10.4271/2004-01-0882.

[15] Schuberth S, Schedin E, Fröhlich T, Ratte E. Next generation vehicle – engineering guidelines for stainless steel in automotive applications. In: Karjalainen P, Hertzman S, editors. 6th Stainl. Steel Sci. Mark. Conf., Helsinki, Finland: Jernkontoret - The Swedish Steel Producers' Association; 2008, p. 637-644 (Paper G02-1).

[16] Qi L, Li F, Zhang Q, Xu Y, Han X, Li Y. Improvement of Single-Sided Resistance Spot Welding of Austenitic Stainless Steel Using Radial Magnetic Field. J Manuf Sci Eng 2021;143:031004. https://doi.org/10.1115/1.4048048.

[17] Sun X, Zhang Q, Wang S, Han X, Li Y, David SA. Effect of adhesive sealant on resistance spot welding of 301L stainless steel. J Manuf Process 2020;51:62–72. https://doi.org/10.1016/j.jmapro.2020.01.033.

[18] Wen J, Wang CS, Xu GC, Zhang XQ. Real time monitoring weld quality of resistance spot welding for stainless steel. ISIJ Int 2009;49:553–6. https://doi.org/10.2355/isijinternational.49.553.

[19] De Tiedra P, Martín Ó, López M, San-Juan M. Use of EPR test to study the degree of sensitization in resistance spot welding joints of AISI 304 austenitic stainless steel. Corros Sci 2011;53:1563–70. https://doi.org/10.1016/j.corsci.2011.01.036.

[20] Barla NA, Ghosh PK, Kumar V, Paraye NK, Anant R, Das S. Simulated stress induced sensitization of HAZ in multipass weld of 304LN austenitic stainless steel. J Manuf Process 2021;62:784–96. https://doi.org/10.1016/j.jmapro.2020.12.061.

[21] Nadimi N, Yadegari R, Pouranvari M. Resistance Spot Welding of Quenching and Partitioning (Q&P) Third-Generation Advanced High-Strength Steel: Process–Microstructure–Performance. Metall Mater Trans A 2023;54:577–89. https://doi.org/10.1007/s11661-022-06903-y.

[22] Bemani M, Pouranvari M. Microstructure and mechanical properties of dissimilar nickel-based superalloys resistance spot welds. Mater Sci Eng A 2020;773:138825. https://doi.org/10.1016/j.msea.2019.138825.

[23] Kianersi D, Mostafaei A, Mohammadi J. Effect of Welding Current and Time on the

Microstructure, Mechanical Characterizations, and Fracture Studies of Resistance Spot Welding Joints of AISI 316L Austenitic Stainless Steel. Metall Mater Trans A 2014;45:4423–42. https://doi.org/10.1007/s11661-014-2421-z.

[24] Kianersi D, Mostafaei A, Amadeh AA. Resistance spot welding joints of AISI 316L austenitic stainless steel sheets: Phase transformations, mechanical properties and microstructure characterizations. Mater Des 2014;61:251–63. https://doi.org/10.1016/j.matdes.2014.04.075.

[25] De Tiedra P, Martín Ó, López M. Combined effect of resistance spot welding and post-welding sensitization on the degree of sensitization of AISI 304 stainless steel. Corros Sci 2011;53:2670–5. https://doi.org/10.1016/j.corsci.2011.05.007.

[26] Gupta RK, Anil Kumar V, Panicker PG. Evaluation of high temperature properties and microstructural characterization of resistance spot welded steel lap shear joints. High Temp Mater Process 2016;35:145–51. https://doi.org/10.1515/htmp-2014-0211.

[27] Monrrabal G, Jiménez JA, Ress J, Fajardo S, Bastidas JM, Llorente I, et al. Corrosion behaviour of resistance-spot-welded high-Mn austenitic TWIP steel. Corros Eng Sci Technol 2021;56:50–9. https://doi.org/10.1080/1478422X.2020.1806606.

[28] Prohaska M, Kanduth H, Mori G, Grill R, Tischler G. On the substitution of conventional corrosion tests by an electrochemical potentiokinetic reactivation test. Corros Sci 2010;52:1582–92. https://doi.org/10.1016/j.corsci.2010.01.017.

[29] De Tiedra P, Martín Ó, San-Juan M. Effect of metallurgical evolution during post-weld aging treatment on localised corrosion of resistance spot welding joints of A286 superalloy. Corros Eng Sci Technol 2018;53:355–61. https://doi.org/10.1080/1478422X.2018.1473318.

[30] Pouranvari M, Marashi SPH. Critical review of automotive steels spot welding: Process, structure and properties. Sci Technol Weld Join 2013;18:361–403. https://doi.org/10.1179/1362171813Y.0000000120.

[31] Shamsolhodaei A, GhateiKalashami A, Safdel A, Midawi ARH, Elbestawi MA, Peng P, et al. Resistance spot welding of NiTi shape memory alloy sheets: Microstructural evolution and mechanical properties. J Manuf Process 2022;81:467–75. https://doi.org/10.1016/j.jmapro.2022.07.006.

[32] Rajarajan C, Sonar T, Sivaraj P, Raja S, Mathiazhagan N. Investigating the Effect of Electrode Pressure on Nugget Size, Microstructure and Tensile Shear Strength of Resistance Spot Welded Advanced High Strength Dual Phase Steel Joints. Metallogr Microstruct Anal 2022;11:472–83. https://doi.org/10.1007/s13632-022-00862-x.

[33] Hafez KM. The effect of welding atmosphere on the pitting corrosion of AISI 304L resistance spot welds. Int J Adv Manuf Technol 2018;97:243–51. https://doi.org/10.1007/s00170-018-1915-z.

[34] Yan B, Lalam SH, Zhu H. Performance Evaluation of GMAW Welds for Four Advanced High Strength Steels. SAE Trans Vol 114, Sect 5 J Mater Manuf 2005:475–85. https://doi.org/10.4271/2005-01-0904.

[35] Alizadeh-Sh M, Marashi SPH. Resistance spot welding of dissimilar austenitic/duplex stainless steels: Microstructural evolution and failure mode analysis. J Manuf Process 2017;28:186–96. https://doi.org/10.1016/j.jmapro.2017.06.005.

[36] Tseng KH, Hsu CY. Performance of activated TIG process in austenitic stainless steel welds. J Mater Process Technol 2011;211:503–12. https://doi.org/10.1016/j.jmatprotec.2010.11.003.

[37] Manladan SM, Yusof F, Ramesh S, Zhang Y, Luo Z, Ling Z. Microstructure and mechanical properties of resistance spot welded in welding-brazing mode and resistance element welded magnesium alloy/austenitic stainless steel joints. J Mater Process Technol 2017;250:45–54. https://doi.org/10.1016/j.jmatprotec.2017.07.006.

[38] Böhni H, Suter T, Schreyer A. Micro- and nanotechniques to study localized corrosion. Electrochim Acta 1995;40:1361–8. https://doi.org/10.1016/0013-4686(95)00072-M.

[39] Böhni H, Suter T, Assi F. Micro-electrochemical techniques for studies of localized processes on metal surfaces in the nanometer range. Surf Coatings Technol 2000;130:80–6. https://doi.org/10.1016/S0257-8972(00)00681-2.

[40] Suter T, Böhni H. A new microelectrochemical method to study pit initiation on stainless steels. Electrochim Acta 1997;42:3275–80. https://doi.org/10.1016/S0013-4686(70)01783-8.

[41] Suter T, Böhni H. Microelectrodes for studies of localized corrosion processes. Electrochim Acta 1998;43:2843–9. https://doi.org/10.1016/S0013-4686(98)00025-5.

[42] Suter T, Böhni H. Microelectrodes for corrosion studies in microsystems. Electrochim Acta 2001;47:191–9. https://doi.org/10.1016/S0013-4686(01)00551-5.

[43] Lohrengel MM. Interface and volume effects in biological cells and electrochemical microcells. Electrochim Acta 1997;42:3265–71. https://doi.org/10.1016/S0013-4686(97)00177-1.

[44] Lohrengel M., Moehring A, Pilaski M. Capillary-based droplet cells: limits and new aspects. Electrochim Acta 2001;47:137–41. https://doi.org/10.1016/S0013-4686(01)00570-9.

[45] Lohrengel M., Rosenkranz C, Klüppel I, Moehring A, Bettermann H, Bossche BV den, et al. A

new microcell or microreactor for material surface investigations at large current densities. Electrochim Acta 2004;49:2863–70. https://doi.org/10.1016/j.electacta.2004.01.068.

[46] Birbilis N, Padgett BN, Buchheit RG. Limitations in microelectrochemical capillary cell testing and transformation of electrochemical transients for acquisition of microcell impedance data. Electrochim Acta 2005;50:3536–44. https://doi.org/10.1016/j.electacta.2005.01.010.

[47] Garcia C, de Tiedra MP, Blanco Y, Martin O, Martin F. Intergranular corrosion of welded joints of austenitic stainless steels studied by using an electrochemical minicell. Corros Sci 2008;50:2390–7. https://doi.org/10.1016/j.corsci.2008.06.016.

[48] Garcia C, Martin F, de Tiedra P, Blanco Y, Lopez M. Pitting corrosion of welded joints of austenitic stainless steels studied by using an electrochemical minicell. Corros Sci 2008;50:1184–94. https://doi.org/10.1016/j.corsci.2007.11.028.

[49] Martín Ó, De Tiedra P, García C, Martín F, López M. Comparative study between large-scale and small-scale electrochemical potentiokinetic reactivation performed on AISI 316L austenitic stainless steel. Corros Sci 2012;54:119–26. https://doi.org/10.1016/j.corsci.2011.09.007.

[50] De Tiedra P, Martín Ó, García C, Martín F, López M. Effect of prior cold work on the degree of sensitisation of welded joints of AISI 316L austenitic stainless steel studied by using an electrochemical minicell. Corros Sci 2012;54:153–60. https://doi.org/10.1016/j.corsci.2011.09.010.

[51] Santos JI, Martín Ó, Ahedo V, de Tiedra P, Galán JM. Glass-box modeling for quality assessment of resistance spot welding joints in industrial applications. Int J Adv Manuf Technol 2022;123:4077–92. https://doi.org/10.1007/s00170-022-10444-4.

[52] ASTM A262-15(2021). Standard practices for detecting susceptibility to intergranular attack in austenitic stainless steels. 2021.

[53] ASTM Standard G108-92. Standard Test Method for Electrochemical Reactivation (EPR) for Detecting Sensitization of AISI Type 304 and 304L Stainless Steels. 1993.

[54] Maday M., Mignone A, Vittori M. The application of the electrochemical potentiokinetic reactivation method for detecting sensitization in inconel 600. The influence of some testing parameters. Corros Sci 1988;28:887–900. https://doi.org/10.1016/0010-938X(88)90037-6.

[55] Matula M, Hyspecka L, Svoboda M, Vodarek V, Dagbert C, Galland J, et al. Intergranular corrosion of AISI 316L steel. Mater Charact 2001;46:203–10. https://doi.org/10.1016/S1044-5803(01)00125-5.

[56] De Tiedra P. Análisis de la influencia del grado de deformación plástica en frío en el comportamiento frente a la corrosión localizada de uniones soldadas de aceros inoxidables austeníticos mediante técnicas macro y microelectroquímicas. PhD Thesis (in Spanish). Universidad de Valladolid, 2010.

[57] Du H, Cheng Y, Hou L, Li Y, Wei Y. Evolution of intergranular corrosion resistance for HR3C heat-resistant austenitic stainless steel at elevated temperature. Corros Eng Sci Technol 2017;52:343–8. https://doi.org/10.1080/1478422X.2017.1291119.

[58] Yu X, Chen S, Liu Y, Ren F. A study of intergranular corrosion of austenitic stainless steel by electrochemical potentiodynamic reactivation, electron back-scattering diffraction and cellular automaton. Corros Sci 2010;52:1939–47. https://doi.org/10.1016/j.corsci.2010.02.015.

[59] Vitek JM, David SA, Hinman CR. Improved Ferrite Number Prediction Model that accounts for Cooling Rate Effects-Part 1: Model Development. Weld J 2003;82:10S-17S.

[60] Vitek JM, David SA, Hinman CR. Improved Ferrite Number Prediction Model that Accounts for Cooling Rate Effects- Part 2 : Model Results. Weld J 2003;82:43S-50S.

[61] Soomro IA, Pedapati SR, Awang M. Optimization of postweld tempering pulse parameters for maximum load bearing and failure energy absorption in dual phase (DP590) steel resistance spot welds. Mater Sci Eng A 2021;803:140713. https://doi.org/10.1016/j.msea.2020.140713.

[62] Gould JE, Khurana SP, Li T. Predictions of microstructures when welding automotive advanced high-strength steels. Weld J 2006;85:111S-116S.

[63] Bansod A V., Patil AP, Moon AP, Khobragade NN. Intergranular Corrosion Behavior of Low-Nickel and 304 Austenitic Stainless Steels. J Mater Eng Perform 2016;25:3615–26. https://doi.org/10.1007/s11665-016-2221-2.

[64] Bhat SD, Vijeesh V, Acharya P, Rao M. Investigation of thin sheet stainless steel resistance spot welds: Effect of weld current on nugget failure and microstructure. Mater Today Proc 2021;35:361–5. https://doi.org/10.1016/J.MATPR.2020.02.350.

[65] Wasnik DN, Dey GK, Kain V, Samajdar I. Precipitation stages in a 316L austenitic stainless steel. Scr Mater 2003;49:135–41. https://doi.org/10.1016/S1359-6462(03)00220-3.

[66] Martín Ó, De Tiedra P, López M, San-Juan M. Combined Effect of Resistance Spot Welding and Post-Welding Sensitization on the Pitting Corrosion Behavior of AISI 304 Stainless Steel. Corrosion 2013;69:268–75. https://doi.org/10.5006/0749.

[67] Zumelzu E, Sepúlveda J, Ibarra M. Influence of microstructure on the mechanical behaviour of welded 316 L SS joints. J Mater Process Technol 1999;94:36–40.

https://doi.org/10.1016/S0924-0136(98)00450-6.

[68] Cui Y, Lundin CD. Austenite-preferential corrosion attack in 316 austenitic stainless steel weld metals. Mater Des 2007;28:324–8. https://doi.org/10.1016/j.matdes.2005.05.022.

[69] Saboori A, Aversa A, Bosio F, Bassini E, Librera E, De Chirico M, et al. An investigation on the effect of powder recycling on the microstructure and mechanical properties of AISI 316L produced by Directed Energy Deposition. Mater Sci Eng A 2019;766:138360. https://doi.org/10.1016/j.msea.2019.138360.

[70] Sabzi M, Dezfuli SM. Drastic improvement in mechanical properties and weldability of 316L stainless steel weld joints by using electromagnetic vibration during GTAW process. J Manuf Process 2018;33:74–85. https://doi.org/10.1016/j.jmapro.2018.05.002.

[71] Li L, Wang Y, Liu J, Chen X, Zhao P, Sun M, et al. Hydrogen transfer behavior and hydrogen affected zone formation of low alloy steel during thermoplastic deformation. J Mater Process Technol 2023;316:117958. https://doi.org/10.1016/j.jmatprotec.2023.117958.

[72] Parthasarathy TA, Shewmon PG. Diffusion induced grain boundary migration in Ni-C alloys. Scr Metall 1983;17:943–6. https://doi.org/10.1016/0036-9748(83)90267-3.

[73] Mishin Y, Herzig C. Grain boundary diffusion: recent progress and future research. Mater Sci Eng A 1999;260:55–71. https://doi.org/10.1016/S0921-5093(98)00978-2.

Figure captions

Fig. 1. Optical micrograph of the FZ of a RSW joint (without post-welding sensitization), which has a cast dendritic microstructure of austenite with delta-ferrite (δ-Fe) in interdendritic regions (electrolytic etching with oxalic acid according to ASTM A262-15(2021) Practice A) [52].

Fig. 2. Optical micrograph of the HAZ of a RSW joint (without post-welding sensitization), in which signs of prior cold work (delta-ferrite (δ-Fe) bands oriented in the rolling direction) are partially removed by the effect of the welding heat input (electrolytic etching with oxalic acid according to ASTM A262-15(2021) Practice A) [52].

Fig. 3. Optical micrograph of the BM of a RSW joint (without post-welding sensitization), which shows an austenitic structure with signs of prior cold work such as delta-ferrite (δ-Fe) bands oriented in the rolling direction (electrolytic etching with oxalic acid according to ASTM A262-15(2021) Practice A) [52].

Fig. 4. (A) Micrometer table on which the sample was clamped. (B) Minicell used in the small-scale EPR tests. (C) Optical macrograph taken in the BM of a RSW joint after a small-scale EPR test to show the size of the exposed working area.

Fig. 5. (A) Location of the small-scale EPR tests in each of the welding zones. The exposed working area is indicated by a circle 0.005 cm^2 in area and 0.8 mm in diameter. in the small-scale EPR tests. The RSW joint shown corresponds to sample No. 10 (electrolytic etching with oxalic acid according to ASTM A262-15(2021) Practice A) [52]. (B) Assessment of repeatability of the small-scale EPR tests: curves obtained from the BM in samples No. 1 (C1 and C2) and No. 0 (C3 and C4).

Fig. 6. In each EPR curve, the reactivation charge Q_r is determined between point A_1 and point A_2 (reactivation hump). Passive layer formation occurs at 200 mV_{sce} (A_0) and the passive layer (passive zone between A_0 and A_1) limits the flow of current until its localized breakdown (A_1) causes the current density to increase significantly. The small-scale EPR curve shown is obtained from the FZ of sample No. 11.

Fig. 7. Small-scale EPR curves obtained from the FZ of: (A) sample No. 0 (Q_r = 0.52144 C/cm^2); (B) sample No. 1 (Q_r = 1.2165 C/cm^2); (C) sample No. 4 (Q_r = 0.37101 C/cm^2); and (D) sample No. 6 (Q_r = 3.4622 C/cm^2).

Fig. 8. Small-scale EPR curves obtained from the HAZ of: (A) sample No. 0 (Q_r = 0.23861 C/cm^2); (B) sample No. 1 (Q_r = 0.69272 C/cm^2); (C) sample No. 4 (Q_r = 0.41732 C/cm^2); and (D) sample No. 6 (Q_r = 0.1602 C/cm^2).

Fig. 9. Small-scale EPR curves obtained from the BM of: (A) sample No. 0 (Q_r = 0 C/cm^2, i.e., there is no reactivation); (B) sample No. 1 (Q_r = 0.14747 C/cm^2); (C) sample No. 4 (Q_r = 0.32757 C/cm^2); and (D) sample No. 6 (Q_r = 0.03397 C/cm^2).

Fig. 10. Small-scale EPR curves obtained from the FZ of: (A) sample No. 0 (Q_r = 0.52144 C/cm^2); (B) sample No. 7 (Q_r = 0.094963 C/cm^2); (C) sample No. 10 (Q_r = 0.25427 C/cm^2); and (D) sample No. 12 (Q_r = 2.1729 C/cm^2).

Fig. 11. Small-scale EPR curves obtained from the HAZ of: (A) sample No. 0 (Q_r = 0.23861 C/cm^2); (B) sample No. 7 (Q_r = 1.9035 C/cm^2); (C) sample No. 10 (Q_r = 0.16359 C/cm^2); and (D) sample No. 12 (Q_r = 10.345 C/cm^2).

Fig. 12. Small-scale EPR curves obtained from the BM of: (A) sample No. 0 (Q_r = 0 C/cm^2, i.e., there is no reactivation); (B) sample No. 7 (Q_r = 1.1744 C/cm^2); (C) sample No. 10 (Q_r = 4.2562 C/cm^2); and (D) sample No. 12 (Q_r = 11.143 C/cm^2).

Fig. 13. Reactivation charge, Q_r (C/cm^2), obtained from each of the welding zones (FZ, HAZ and BM) of the RSW joint without post-weld sensitization (sample No. 0, which has no reactivation in the BM, i.e., with Q_r = 0 C/cm^2) and of the six RSW joints subjected to post-weld sensitization at 675 ºC (samples Nos. 1 to 6).

Fig. 14. Reactivation charge, Q_r (C/cm^2), obtained from each of the welding zones (FZ, HAZ and BM) of the RSW joint without post-weld sensitization (sample No. 0, which has no reactivation in the BM, i.e., with Q_r = 0 C/cm^2) and of the six RSW joints subjected to post-weld sensitization at 750 ºC (samples Nos. 7 to 12).

Fig. 15. Optical micrographs (electrolytic etching with oxalic acid according to ASTM A262-15(2021) Practice A [52]) of: (A) FZ of sample No. 1; (B) FZ of sample No. 4; (C) FZ of sample No. 6; (D) HAZ of sample No. 1. (E) HAZ of sample No. 4; (F) HAZ of sample No. 6; (G) BM of sample No. 1; (H) BM of sample No. 4; (C) BM of sample No. 6.

Fig. 16. Optical micrographs (electrolytic etching with oxalic acid according to ASTM A262-15(2021) Practice A [52]) of: (A) FZ of sample No. 7; (B) FZ of sample No. 10; (C) FZ of sample No. 12; (D) HAZ of sample No. 7. (E) HAZ of sample No. 10; (F) HAZ of sample No. 12; (G) BM of sample No. 7; (H) BM of sample No. 10; (C) BM of sample No. 12.

Fig. 17. (A) EDX line scan between two dendrites for Cr content in the FZ of sample No. 12; although the electrolytic etching with oxalic acid, according to ASTM A262-15(2021), dissolves the chromium-rich phases that had precipitated along interdendritic regions, the chromium depleted zones, adjacent to the chromium-rich phases, are shown. (B) SEM micrograph of the line scan location.